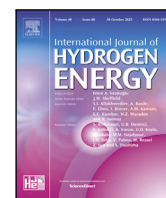




Contents lists available at ScienceDirect

International Journal of Hydrogen Energy

journal homepage: www.elsevier.com/locate/hydro

Direct numerical simulations with multi-step chemistry of liquid water interaction with laminar spherically expanding premixed hydrogen/air flames

Riccardo Concetti¹*, Josef Hasslberger¹, Markus Klein¹

Department of Aerospace Engineering, University of the Bundeswehr Munich, Werner-Heisenberg-Weg 39, Neubiberg, 85577, Germany

ARTICLE INFO

Keywords:

Direct numerical simulations
Hydrogen/air premixed combustion
Intrinsic flame instabilities
Flame-water interaction

ABSTRACT

In the present study, the behavior of laminar spherically expanding premixed hydrogen/air flame interacting with liquid water droplets is investigated through direct numerical simulations. A hybrid Eulerian–Lagrangian approach with two-way coupling is employed for the numerical representation of the problem, and the droplets are modeled as point sources. The effects of equivalence ratio, initial droplet diameter, and multi-species diffusion model variation are analyzed. Results indicate that an accurate description of the diffusion process is crucial at low equivalence ratios due to the strong influence of thermodynamic properties, but becomes less significant at higher equivalence ratios. Additionally, the Soret effect enhances flame speed and susceptibility to intrinsic flame instabilities onset at low equivalence ratios, while contributing to flame stability in higher equivalence ratio conditions. However, the introduction of water droplets significantly alters the Soret effect's influence by modifying H radical production and distribution. Furthermore, water addition is found to increase flame area generation, yet simultaneously reduces the burning rate per unit area of the flame. Lastly, the impact of water addition on emissions is assessed, revealing that, in the configuration considered, water enhances nitrogen oxide production by influencing the N_2O pathway, which is triggered by the presence of H and O radicals. This pathway becomes more prominent at lower temperatures due to its insensitivity to temperature. In this context, nitrogen monoxide production is promoted in the presence of strongly localized “cold spots”, aided by water evaporation, which increase radical concentration, as well as by the high collision efficiency of water, which is important for initiating the N_2O pathway.

1. Introduction

In recent years, regulations on emissions have become increasingly stringent. In response, there has been renewed interest within the research community in exploring the potential of liquid water injection in combustion devices [1–3]. The effects of liquid water on flames are primarily linked to cooling, as water evaporation extracts heat, as well as the dilution of reactants—where the presence of steam reduces the concentration of fuel and oxidizer, thereby decreasing the heat release per unit mass. Additionally, there are chemical effects from water molecule's high collision efficiency, which influences radical production and flame structure. These three mechanisms together contribute to a potential reduction in NO_x emissions, primarily due to a significant decrease in flame temperature, and also due to effects on radical production and consumption, as demonstrated by Concetti et al. [4] for 1D laminar premixed hydrogen/air flames.

Beyond emission reduction, this technology has been historically considered, as it can increase the power output of combustion systems

by increasing the mass flow through the system. Examples include the Pratt & Whitney J57 wet engine and the 1962 Oldsmobile Jetfire. Moreover, experimental and computational studies have demonstrated performance improvements and emissions reduction, particularly with respect to NO_x , in diesel engines and gas turbines when employing this technique [5–7]. Furthermore, liquid water-flame interaction is significant in the context of safety systems for fire suppression and explosion mitigation. Various numerical and experimental studies have demonstrated the effectiveness of water in reducing pressure rising in case of explosions and its potential for suppressing accidental fires, particularly when combined with additives [8,9].

In recent decades, combustion research has increasingly focused on carbon-free fuels, with hydrogen being the main example. Hydrogen offers several advantages, including its intrinsic renewability and high energy density by mass (i.e., 141 MJ/kg). However, using hydrogen presents challenges, such as its low boiling point, which complicates

* Corresponding author.

E-mail addresses: riccardo.concetti@unibw.de (R. Concetti), josef.hasslberger@unibw.de (J. Hasslberger), markus.klein@unibw.de (M. Klein).

<https://doi.org/10.1016/j.ijhydene.2025.02.286>

Received 25 November 2024; Received in revised form 22 January 2025; Accepted 18 February 2025

Available online 8 March 2025

0360-3199/© 2025 The Authors. Published by Elsevier Ltd on behalf of Hydrogen Energy Publications LLC. This is an open access article under the CC BY license (<http://creativecommons.org/licenses/by/4.0/>).

storage in liquid form, and its low volumetric density, which necessitates large storage volumes. Additionally, hydrogen's broad flammability range and high flame speed raise safety concerns, particularly in the event of leaks or flashback, which have been extensively studied [10–12].

Specifically, hydrogen exhibits a high unstretched laminar burning velocity, $S_L \approx 2.5$ m/s for a stoichiometric hydrogen/air mixture at atmospheric conditions, compared to $S_L \approx 0.4$ m/s for a methane/air mixture under the same conditions. This discrepancy is further amplified when the flame is subjected to stretch. When a flame is stretched, it tends to wrinkle and form curved structures, this phenomenon is strengthened in presence of intrinsic instabilities. These intrinsic flame instabilities are inherent to the flame and mixture properties, such as the density jump across the flame, activation energy, and diffusion characteristics, as defined by Matalon [13], and are independent of external factors. The study of intrinsic flame instabilities began nearly a century ago with the pioneering work of Darrieus [14] and Landau [15], who independently described the occurrence of flame front instability in perturbed flames. The theory behind these phenomena was further developed, with numerous studies available in the literature [16–18]. Many attempts have been made to define a general and valid dispersion relation—an analytical expression linking the wavelength of flame front disturbances to their growth rate. However, the validity of the most widely accepted dispersion relations [19–23] is limited to a high density jump across the flame and Lewis number of the mixture close to unity, or to an almost absent density jump across the flame and Lewis number of the mixture far from unity, where the Lewis number represents the ratio of thermal to mass diffusivity. Since lean hydrogen/air mixtures, which are of practical importance today, fall outside the valid range of the previously considered dispersion relations due to their high density jump and extremely low Lewis number, ongoing efforts are focused on developing new analytical formulations to describe the behavior of these mixtures [24–26].

Spherically expanding flames represent a typical scenario in practical combustion, where ignition occurs locally and the flame propagates outward. Such flames, characterized by non-zero mean curvature, are inherently stretched. Consequently, they often exhibit the cellular structure typical of intrinsically unstable flames [27,28]. The appearance of these structures depends on the growth rate of disturbances, which must surpass the radial expansion rate of the flame to become visible; otherwise, the cellular structures are flattened by the propagation of the flame front. Addabbo et al. [29] described the behavior of a general spherically expanding flame, finding that as the flame radius increases, the range of unstable modes also increases. The critical radius corresponds to the minimum radius at which at least one unstable mode emerges. Once an unstable disturbance is established, it grows indefinitely, with the cellular structures fragmenting into smaller cells as the wavenumber of unstable modes increases. For mixtures with low Lewis numbers, spherically expanding flames tend to exhibit instability soon after ignition, and this behavior is consistent with Addabbo's findings. In literature there are several investigations of flame instability development for purely gaseous spherically expanding flames [27,28,30,31], which confirm the exposed theory. The presence of liquid water, through its cooling and dilution effects, impedes flame propagation, causing the flame front to wrinkle around evaporating water droplets. If these localized deformations are sufficiently intense and distant, they can trigger unstable modes, potentially growing indefinitely. This phenomenon has been investigated numerically for hydrocarbon/air planar premixed flames with an ordered array of water droplets [32]. However, evaporating water also exerts a strong cooling effect, which reduces the burning rate per unit area. Thus, both increased flame surface area and decreased burning rate coexist, and their relative dominance depends on the droplet cloud conditions. To the best of the author's knowledge, the literature has not fully addressed under which conditions one of these factors predominates.

This paper aims to explore several open aspects through the use of direct numerical simulations to analyze the effects of liquid water addition on global flame characteristics, but also to examine the impact of different diffusion models – mixture-averaged, multi-component diffusion, and multi-component diffusion with the Soret effect – on flame stability. In low Reynolds number flows, diffusion effects are significant, and accurate modeling is essential. Previous studies have shown discrepancies in local flame speed predictions between the mixture-averaged and multi-component diffusion models, with differences of up to 30% in certain regions of curved flames when light fuels, such as hydrogen, are used [33]. The Soret effect (denoting species transport due to temperature gradients), which can enhance or reduce flame speed depending on the fuel, is particularly relevant to hydrogen combustion, where molecular and atomic hydrogen tend to diffuse toward the burned region, increasing flame speed. In contrast, heavier fuels experience the opposite effect [34–36].

Additionally, we investigate the potential of liquid water injection for NO_x reduction, a toxic and climate-relevant pollutant whose formation is strongly influenced by temperature and radical distribution. Flame topology and local structure can significantly impact NO_x production, as observed in DNS studies of thermodynamically unstable flames [37]. In hydrogen combustion, the behavior of atomic hydrogen and oxygen radicals, which are highly concentrated in the post-flame region of curved flame fronts, promotes NO_x formation via the NNH or N₂O pathway, the primary nitrogen formation routes after the thermal pathway [4,7,38]. Water injection has the potential to reduce local temperatures, but its effects on radical concentrations and flame topology also influence NO_x production.

The objectives of this study are the following:

1. to assess how different diffusion models affect flame stability and global flame characteristics;
2. to examine the effects of liquid water addition on global flame characteristics such as flame surface area and burning rate;
3. to analyze the onset of intrinsic flame instabilities, which manifest as cellular structures on the flame surface;
4. to investigate the effects of water addition on NO_x production in hydrogen/air combustion;

The following section will introduce the mathematical background, followed by a presentation of the numerical framework. In Section 4, the results are presented and discussed. Finally, the conclusions are outlined in Section 5.

2. Mathematical background

The present study analyzes the interaction of liquid water droplets with hydrogen/air premixed combustion under quasi-laminar conditions. A hybrid Eulerian–Lagrangian approach with two-way coupling is employed. In this approach, the gas phase is solved using the standard conservation equations for mass, momentum, chemical species and energy. Specifically, energy is solved for the specific total enthalpy $H_s = h_s + |\bar{u}|^2/2$, which is the sum of the specific sensible enthalpy h_s and the specific kinetic energy $|\bar{u}|^2/2$. Simultaneously, the liquid phase is represented as a collection of droplets modeled as point sources. The droplets are tracked along their trajectories within the domain, and their evolution in terms of mass, position, velocity, and temperature is computed over time. This approach is justified since the droplets are significantly smaller than the grid resolution (with initial droplet diameters $a_d = 7 - 14$ μm, compared to a grid resolution of 33 μm). Furthermore, the average droplet spacing $s_d = 234 - 662$ μm, comparable to the stoichiometric thermal flame thickness $\delta_{st} \approx 350$ μm, ensures that droplet–droplet interactions are highly improbable. This approach has been successfully employed in several studies in the literature [39–42]. The governing equations for the gas phase are as follows:

- mass conservation equation

$$\frac{\partial \rho}{\partial t} + \nabla \cdot (\rho \vec{u}) = \dot{S}_\rho \quad (1)$$

- momentum conservation equation

$$\frac{\partial(\rho \vec{u})}{\partial t} + \nabla \cdot (\rho \vec{u} \vec{u}) = -\nabla p + \nabla \cdot \tau + \dot{S}_u \quad (2)$$

- energy conservation equation

$$\frac{\partial \rho (h_s + |\vec{u}|^2/2)}{\partial t} + \nabla \cdot (\rho \vec{u} (h_s + |\vec{u}|^2/2)) = -\nabla \cdot \vec{q} + \frac{\partial p}{\partial t} - \sum_k h_k^0 \dot{\omega}_k + \dot{S}_h \quad (3)$$

- species conservation equation

$$\frac{\partial(\rho Y_k)}{\partial t} + \nabla \cdot (\rho (\vec{u} + \vec{u}_c) Y_k) = \dot{\omega}_k - \nabla \cdot \vec{j}_k + \dot{S}_{Y_k} \quad (4)$$

The mass conservation equation solves for gas density ρ and couples it with the velocity \vec{u} . In the momentum equation, the pressure gradient p and viscous forces, represented by the shear stresses τ , are included. The shear stresses are computed using the Newtonian constitutive equation:

$$\tau = \mu [\nabla \vec{u} + (\nabla \vec{u})^T - \frac{2}{3} \mathbf{I} \nabla \cdot \vec{u}] \quad (5)$$

where μ is the dynamic viscosity, and \mathbf{I} is the identity matrix. The energy equation accounts for diffusion via the term:

$$-\nabla \cdot \vec{q} = \nabla \cdot \left(\frac{\lambda}{c_p} \nabla h_s \right) - \sum_k \nabla \cdot \left(\frac{\lambda}{c_p} h_{s,k} \nabla Y_k \right) - \sum_k \nabla \cdot (h_{s,k} \hat{j}_k) \quad (6)$$

where λ is the thermal conductivity, and c_p is the specific heat at constant pressure of the mixture. The sensible enthalpy of species k , $h_{s,k} = h_k - h_k^0$, is defined relative to the species' enthalpy of formation h_k^0 . The species conservation equation, which computes the mass fractions Y_k , uses a correction velocity \vec{u}_c to ensure that the sum of the diffusive mass fluxes \vec{j}_k equals zero, and it is computed as $\vec{u}_c = -1/\rho \sum_k \vec{j}_k$. Two main diffusion models are considered, which are the mixture-averaged diffusion [43], and multi-component diffusion [44]. The latter has been considered with and without thermophoretic effect (Soret effect), known to be significant in lean hydrogen/air combustion [26,45–47]. In the mixture-averaged approach, the diffusive flux is given by:

$$\vec{j}_k = -\rho D_{m,k} \nabla Y_k - Y_k \rho D_{m,k} \frac{1}{M} \nabla \bar{M} \quad (7)$$

where $D_{m,k}$ is the species k 's diffusion coefficient in the mixture, and \bar{M} is the mixture's average molar mass. The diffusion coefficient $D_{m,k}$ is calculated as:

$$D_{m,k} = \frac{1 - Y_k}{\sum_{i \neq k} \frac{X_i}{D_{k,i}}} \quad (8)$$

For the multi-component diffusion, which is more accurate but computationally more expensive than the mixture-averaged diffusion, the diffusive mass flux of species k is calculated as:

$$\begin{aligned} \vec{j}_k &= \rho \frac{M_k}{M} \sum_{i \neq k} D_{k,i} \nabla Y_i - \rho M_k \sum_{i \neq k} (Y_i D_{k,i}) \nabla \left(\frac{1}{M} - \frac{Y_k}{M_k} \right) \\ &\quad - \rho \sum_{i \neq k} (Y_i D_{k,i}) \nabla Y_k - D_k^T \frac{1}{T} \nabla T \end{aligned} \quad (9)$$

Here, M_k is the molar mass of species k . The final term represents the Soret effect, where mass fluxes are induced by temperature gradients. In the energy and species balance equations, the reaction rate $\dot{\omega}_k$ is included, accounting for the effects of each elementary reaction on species production and consumption. The heat release due to chemical reactions is determined using Hess' law, based on the difference in enthalpy of formation between products and reactants. Thermodynamic properties, such as specific heat and enthalpy, are computed using NASA's 7th-order polynomials, while transport coefficients are obtained via Chapman–Enskog kinetic theory [48]. The right-hand

side of the balance equations contains source terms \dot{S}_ρ , \dot{S}_u , \dot{S}_h , and \dot{S}_{Y_k} , representing the effect of the liquid phase on the gaseous phase. These source terms are calculated from the time variation of volume-averaged droplet properties within each computational cell ($\dot{S}_\rho = d(1/N_d \sum_k \varphi_k)/dt$, where φ is a general droplet's property, N_d is the number of droplets in the cell and the sum is over the droplets). The evolution of droplet properties is governed by the following system of ordinary differential equations:

$$\begin{aligned} \frac{d\vec{x}_d}{dt} &= \vec{u}_d; & \frac{d\vec{u}_d}{dt} &= \frac{3\mu C_d}{4\rho_d a_d^2} [\vec{u}(\vec{x}_d, t) - \vec{u}_d]; \\ \frac{dT_d}{dt} &= [T(\vec{x}_d, t) - T_d + \frac{\dot{m}_d L_v}{4\pi a_d^2 h}] \frac{6h}{\rho_d a_d c_p^l}; \\ \frac{dm_d}{dt} &= k_m (N^s - N^\infty) \pi a_d^2 \bar{M} \end{aligned} \quad (10)$$

where subscript d denotes droplet properties (e.g., ρ_d , a_d). The equation for droplet velocity includes only the drag force, with the drag coefficient C_d computed as [49]:

$$C_d = \begin{cases} 24(1 + Re_d^{2/3}/6) & \text{if } Re_d \leq 1000 \\ 0.424 Re_d & \text{if } Re_d > 1000 \end{cases} \quad (11)$$

where Re_d is the droplet Reynolds number. The heat and mass transfer coefficients h and k_m are determined using the Nusselt and Sherwood numbers, respectively, through the Ranz–Marshall correlation [50]:

$$Nu = 2 + 0.6 Re_d^{1/2} Pr^{1/3}; \quad Sh = 2 + 0.6 Re_d^{1/2} Sc^{1/3} \quad (12)$$

The number of moles at saturation N^s and at the interface N^∞ are calculated using the 1/3 rule [51,52]. The equation for droplet temperature includes the latent heat of vaporization L_v and the specific heat of the liquid phase c_p^l . The two-way coupling implementation is evident in the equations presented thus far, where terms related to the other phase are present in the equations.

In this study, the use of a progress variable is considered for collecting statistics, which indicates the extent of reaction and is a widely used concept in the literature [42,53–55]. While the deficient reactant is typically used for simplified chemistry, for detailed chemistry, various combinations of species are employed. In this work, the mass fraction of hydrogen is chosen to define the progress variable. Other options were unsuitable due to the influence of water on their values. Additionally, oxygen was excluded because it is never the limiting reactant, in the cases considered, and its field is less sensitive to flame stretch evolution, hiding some relevant phenomena. Hence, the progress variable is defined as follows:

$$c = \frac{Y_{H_2}^b - Y_{H_2}}{Y_{H_2}^b - Y_{H_2}^u} \quad (13)$$

where the superscripts u and b stand for initial and equilibrium conditions, respectively.

3. Numerical implementation

The code utilized in the present study is a modified version of EBI-DNS solver [56], which incorporates also the Lagrangian phase. The code has been developed within the OpenFOAM computational framework and employs the finite volume method (FVM). Spatial discretization is conducted at second-order accuracy through the Gaussian integration and a linear interpolation of the quantities between the cell centers for both convective and diffusive terms. Time advancement is performed with a variable time step, depending on a sufficiently small maximum Courant number, and it is handled implicitly using a first order accuracy level in conjunction with the PIMPLE algorithm. PIMPLE is an algorithm used to solve the pressure–velocity coupling [57]. It combines the SIMPLE (Semi-Implicit Method for Pressure Linked Equations) and PISO (Pressure-Implicit with Splitting of Operators) algorithms and consists of one inner and one outer loop. The inner

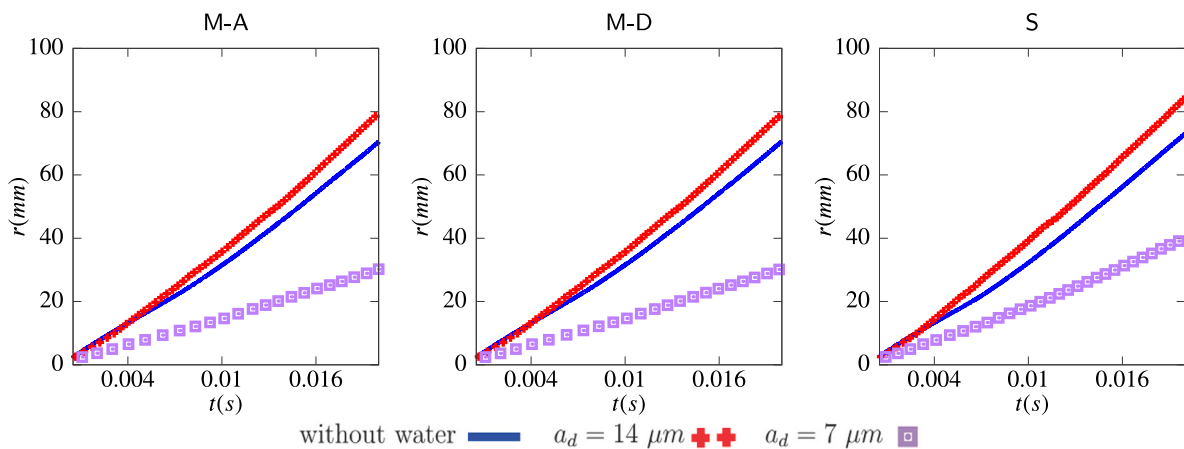


Fig. 1. Time evolution of the flame radius r for the cases with equivalence ratio $\phi = 0.5$. In the left column, the results for the cases with the mixture-averaged model (M-A) are reported; in the central column, the cases with multi-component diffusion (M-D); and in the right column, the cases with multi-component diffusion including the Soret effect (S).

loop corrects the velocity field prediction by adjusting the pressure through the solution of the Poisson equation. The outer loop computes a velocity prediction based on the pressure field obtained either from the previous time step or from the inner loop. Chemical kinetics is computed through Cantera [58], which is coupled with the OpenFOAM code. This coupling allows Cantera to calculate reaction rates, transport properties, and thermodynamic properties for every control volume, which are then passed back to the EBI-DNS solver. The chemical mechanisms considered in this study include the Li mechanism [59] (9 species and 21 elementary reactions) for full flame evolution cases, and the CRECK mechanism [60–62] (31 species and 203 elementary reactions) for the analysis of NO_x emissions. The modified code has been validated by reproducing the simulations conducted in the work of Gai et al. [63]. A comparison of the results for laminar flame speed, temperature, and heat release rate shows that the values resemble closely those in literature, confirming the reliability of the present implementation. These values are reported in the appendix of this work. A two-dimensional (2D) configuration was chosen, as the flow under consideration is quasi laminar, and allows to dedicate more computational resources for a detailed description of the chemistry. The computational domain is a square, measuring 20 cm \times 20 cm, and is discretized with a cell size of 33 μm . This resolution ensures that at least 10 grid cells are available to capture the flame structure. The initial conditions assume a quiescent flow and unburned state throughout the domain, except for a small circular region with a radius of 0.5 mm at the center, where thermodynamic equilibrium conditions are applied. Boundary conditions are defined as outflow conditions, impeding inflow, fixed pressure at 1 atmosphere (the nominal pressure for the simulations), and zero-gradient conditions for both temperature and chemical species. The simulations in the dataset consider unburned gas temperatures of 300 K and a pressure of 1 atm for all cases. Two equivalence ratios, 0.5 and 0.8, are analyzed, while cases with water addition feature a water loading of 10% by mass. The initial droplet temperature is also set at 300 K. The droplets are randomly distributed throughout the domain, with the exception of the central region with the gas at thermochemical equilibrium conditions.

4. Results

4.1. Effects of diffusion model on propagation characteristics

The three diffusion models considered in this study are the mixture-averaged diffusion, the multi-component diffusion, and the multi-component diffusion with the inclusion of the Soret effect, referred to as M-A, M-D, and S, respectively. The latter model is the most accurate but also the most computationally expensive. As previously noted,

significant differences among these models can emerge primarily under lean hydrogen/air combustion conditions. An additional complexity in the present work is the inclusion of evaporating water droplets, which can create localized strong temperature gradients. Fig. 1 illustrates the temporal evolution of the flame radius (r) for the various simulated cases with an equivalence ratio of $\phi = 0.5$. It can be observed that the M-A and M-D models exhibit very similar behavior, thereby supporting the validity of the mixture-averaged approximation. Conversely, the inclusion of the Soret effect results in faster flame propagation for all cases, both with and without water addition, and for both droplet sizes, leading to a somewhat higher values of r at the end of the simulations. The relative differences between the diffusion models become more pronounced with water droplets addition, particularly for large droplets, where the disturbance caused by the droplets accelerates the flame propagation. These findings confirm those in the literature [36], indicating that the Soret effect can amplify flame instabilities by promoting the development of cellular structures, that are naturally formed once the flame radius is higher than the critical value, which can be predicted through the theory proposed by Addabbo et al. [29]. The generation and amplification of cellular structures are further enhanced by the flame interaction with evaporating water droplets. The consumption speed of a spherically expanding laminar flame, as established in the literature [64], can be expressed as:

$$S_c = \left[1 + \frac{1}{2} \frac{\delta_z}{r} \left(1 + \frac{\rho^u}{\rho^b} \right) \right] \frac{\rho^b}{\rho^u} \frac{dr}{dt} \quad (14)$$

where δ_z is the Zeldovich flame thickness, defined as $\delta_z = \lambda / (\rho c_p S_{L,(\phi)}^0)$, with $S_{L,(\phi)}^0$ denoting the unstretched laminar flame speed for the equivalence ratio ϕ , and superscripts u and b referring to unburned and burned states, respectively. This expression accounts for a finite flame thickness, but in the current simulations, once the flame radius becomes much larger than the flame thickness, the expression for the consumption speed simplifies to the time derivative of the flame radius, weighted by the density ratio across the flame. Accordingly, the time evolution of the flame radius r can be correlated to the consumption speed. As shown in several studies [24,42,65], the consumption speed can be further decomposed into contributions from the flame area (A_c) and the burning rate per unit area (Ω). Strictly speaking, the flame area in the context of a 2D simulation should be referred to as a flame length and similar for other quantities. However, the authors have chosen to retain the nomenclature typically used for three-dimensional configurations to maintain consistency with standard technical terminology. The flame area is computed through the flame surface density function $|\nabla c|$ as the integral in the entire domain of this quantity ($A_c = \int |\nabla c| dV$). This is a standard method in combustion DNS [66] and has been shown in [66] to be more robust than isocontour based flame area evaluation.

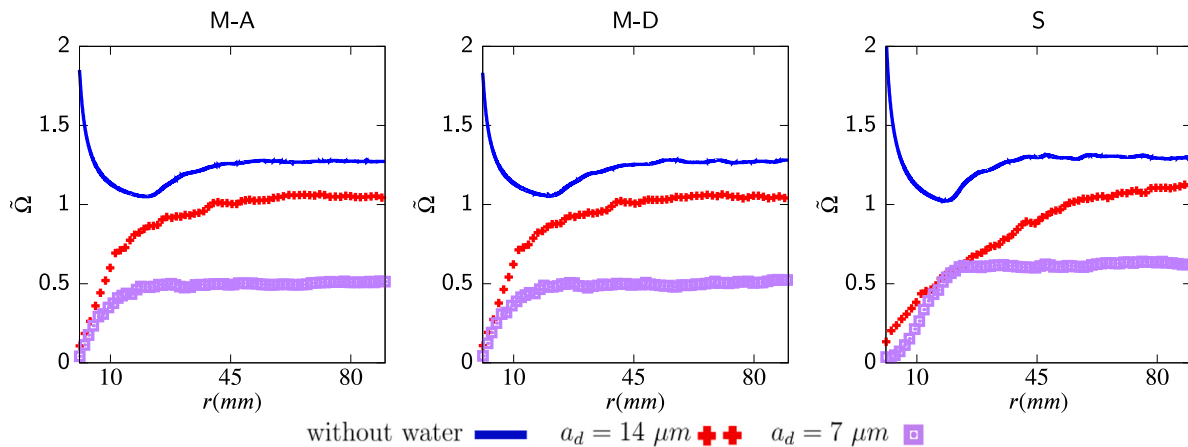


Fig. 2. Evolution of the normalized burning rate per unit area $\tilde{\Omega}$ versus the flame radius r for the cases with equivalence ratio $\phi = 0.5$. In the left column, the results for the cases with the mixture-averaged model (M-A) are reported; in the central column, the cases with multi-component diffusion (M-D); and in the right column, the cases with multi-component diffusion including the Soret effect (S).

At the same time, the burning rate per unit area of the flame is defined as:

$$\Omega = \frac{\int_V \dot{\omega}_c dV}{\int_V |\nabla c| dV} \quad (15)$$

The reaction rate inside the integral is related to the progress variable and it is equal to $\dot{\omega}_c = \dot{\omega}_{H_2} / (Y_{H_2}^b - Y_{H_2}^u)$. In the case of a laminar unstretched flame with unity Lewis number and adiabatic conditions, Ω simplifies to $\rho^u S_{L,c}^0$, following Damköhler's first hypothesis [67,68]. However, under the present conditions, none of these assumptions hold, and deviations from the theoretical results are expected. Fig. 2 presents the normalized burning rate per unit area $\tilde{\Omega} = \Omega / (\rho^u S_{L,c}^0)$ for the different diffusion models and water droplet configurations. The effect of droplet addition consistently reduces the burning rate per unit area across all cases considered. This reduction is more pronounced when smaller droplets are injected compared to larger ones because of faster evaporation of smaller droplets. During the initial ignition transient, the evaporation of water droplets competes with the dissociation reaction of H_2 , both of which are endothermic. As a result, the burning rate per unit area of the flame is high for the cases without water droplets, while it is close to zero for the cases with droplets addition. Moreover, the impact of different diffusion models on this quantity is minimal, except when the Soret effect is accounted for, where a more significant influence is observed, particularly in the presence of water droplets. The observed variations can be attributed to the accelerated radial expansion in cases involving the Soret effect, resulting in reduced interaction time between the flame and droplets. Additionally, the local temperature rise, typically induced by the Soret effect, which promotes the diffusion of H and H_2 toward the flame under conditions of strong preferential diffusion, also plays a positive role. This temperature elevation is associated with the differential diffusion of H and H_2 in the reaction zone [35,36]. It is evident that, for the case with $\phi = 0.5$, preferential diffusion increases the normalized burning rate per unit area to a value of approximately 1.3. The other primary factor influencing the consumption speed is the flame area. For lean hydrogen/air mixtures in a spherical expanding flame configuration, cellular structures naturally emerge due to intrinsic flame instabilities. At an equivalence ratio of $\phi = 0.5$, as predicted by Addabbo's dispersion relation, diffusion fails to stabilize the flame, and cellular structures are initiated by thermodiffusive instability. In this context, the diffusion model is expected to significantly influence the extent of instability. Fig. 3 shows the evolution of the flame area A_c non-dimensionalized with the area of the initial flame kernel at equilibrium conditions for the different diffusion models and water droplet dimension at $\phi = 0.5$. The flame area of the initial kernel A_0 has been selected as normalizing parameter as it shows the area generation from both

the kernel expansion and the flame surface wrinkling, and it is the same in all the different cases. The flame area is positively influenced by the presence of water droplets of both sizes across all diffusion models. However, while the increase in flame area is sufficient for the cases with large droplets to achieve a higher consumption speed compared to the cases without water addition, the same does not hold for the simulations with small droplets, where the cooling effect dominates, resulting in a significantly lower consumption speed than in the absence of water addition (see Fig. 1). Analyzing the evolution of the flame area further emphasizes the differences among the three diffusion models, with the most notable discrepancy arising when the Soret effect is accounted for. It is clear that the Soret effect not only influences the flame evolution directly but also through its interaction with the water droplets. The divergence in flame area between cases with large and small droplets is substantial only when the Soret effect is included, likely due to variations in local temperature gradients. Large droplets, which require more time to evaporate, induce "cold spots" and localized temperature gradients that are more pronounced due to limited time for diffusive processes to homogenize these effects. In contrast, smaller droplets evaporate more rapidly, allowing sufficient time for diffusion to homogenize temperature perturbations. Consequently, the intensity of localized temperature gradients is reduced when small droplets are present, thereby diminishing the impact of the Soret effect in promoting the formation of cellular structures on the flame surface. These observations suggest that, in lean hydrogen/air combustion, the Soret effect notably enhances cellular instability. Furthermore, the injection of liquid water accentuates the discrepancies between cases with and without the Soret effect, particularly when droplet evaporation induces strong localized temperature gradients, as seen with large water droplets.

The current analysis has focused on the influence of the Soret effect in lean hydrogen/air mixtures. However, it is relevant to investigate whether these findings hold when preferential diffusion is less significant, as in the case of an equivalence ratio of $\phi = 0.8$. Fig. 4 shows the time evolution of the flame radius for cases with an equivalence ratio of $\phi = 0.8$. The results for the cases with equivalence ratio $\phi = 0.8$ show a trend opposite to that observed for the leaner case ($\phi = 0.5$) without water addition with respect to transport modeling (compare Fig. 1). When the Soret effect is considered, the flame reaches the domain boundary at a later time. Meanwhile, the cases with small water droplets are consistent with the trends seen previously for $\phi = 0.5$, where the case with Soret effect inclusion expands faster than the other cases. The reason behind this difference, in the absence of water, lies in the altered distribution of radicals, particularly atomic hydrogen (H), when the Soret effect is active, as also observed in

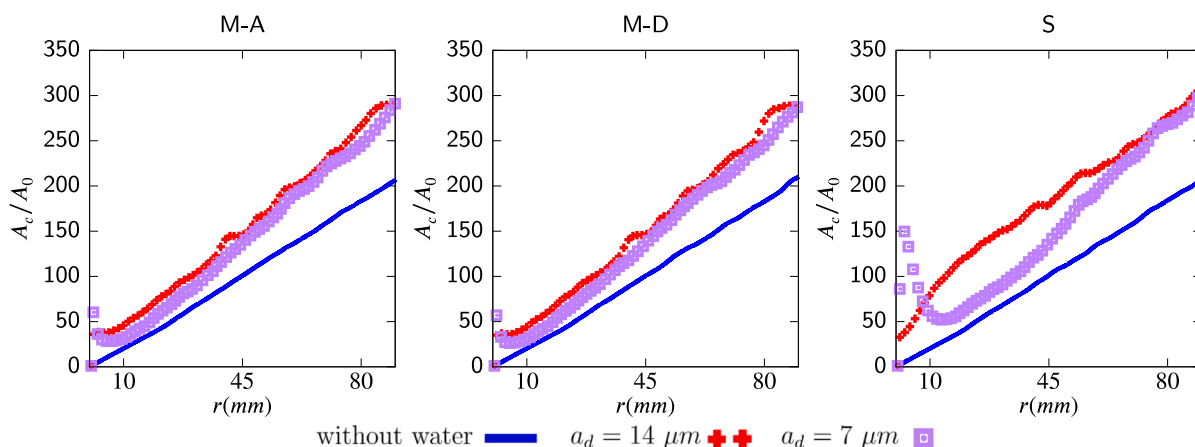


Fig. 3. Evolution of the non-dimensionalized flame area A_c/A_0 versus the flame radius r for the cases with equivalence ratio $\phi = 0.5$. In the left column, the results for the cases with the mixture-averaged model (M-A) are reported; in the central column, the cases with multi-component diffusion (M-D); and in the right column, the cases with multi-component diffusion including the Soret effect (S).

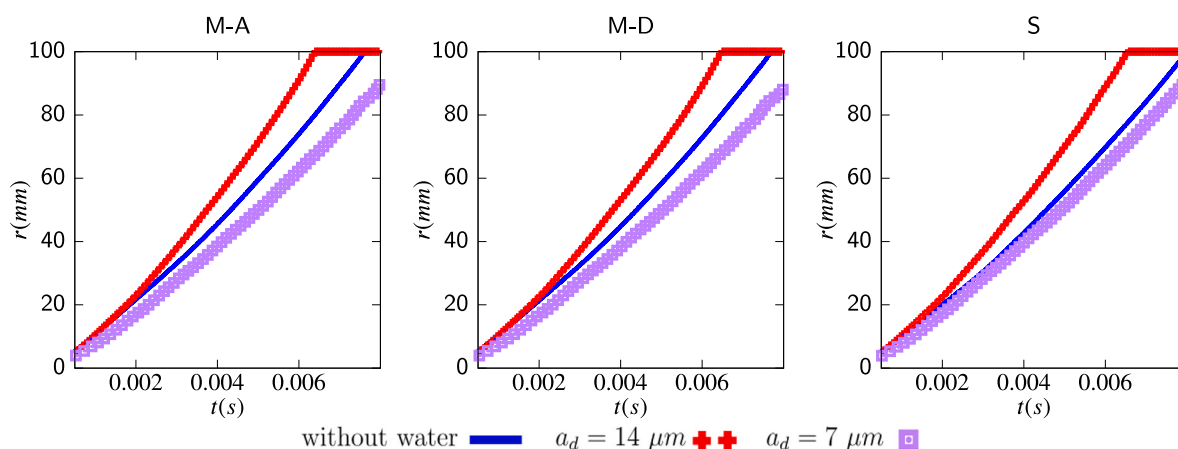


Fig. 4. Time evolution of the flame radius r for the cases with equivalence ratio $\phi = 0.8$. In the left column, the results for the cases with the mixture-averaged model (M-A) are reported; in the central column, the cases with multi-component diffusion (M-D); and in the right column, the cases with multi-component diffusion including the Soret effect (S).

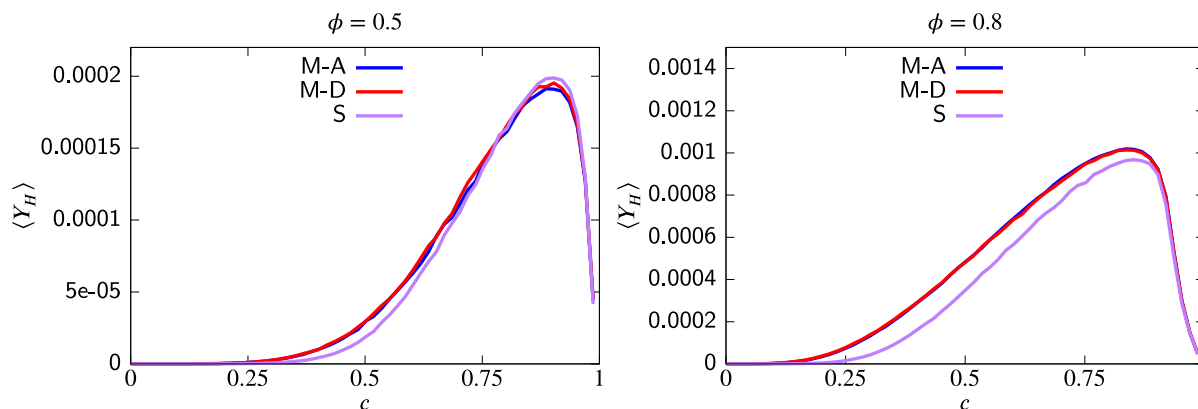


Fig. 5. Average of atomic hydrogen mass fraction $\langle Y_H \rangle$ conditional on the progress variable c for cases with equivalence ratios $\phi = 0.5$ (left) and $\phi = 0.8$ (right) without water droplets. The statistics are taken at $t = 0.02$ s for $\phi = 0.5$ and at $t = 0.006$ s for $\phi = 0.8$. The blue curves represent the cases with mixture-averaged diffusion (M-A), the red curves represent the cases with multi-component diffusion (M-D), and the purple curves represent the cases with the inclusion of Soret effect (S). (For interpretation of the references to color in this figure legend, the reader is referred to the web version of this article.)

literature [33,45,69,70]. The activation of the Soret effect results in a narrower distribution of H, with increased peak values for the lean case ($\phi = 0.5$), as shown on the left side of Fig. 5, where the average of the H mass fraction $\langle Y_H \rangle$, conditional on the progress variable is reported. For the higher equivalence ratio considered ($\phi = 0.8$), the peak value of

the radical concentration decreases in the presence of the Soret effect compared to cases without it. This reduction in radical concentration reflects for the slower flame propagation observed in the $\phi = 0.8$ case with the Soret effect without water addition, compared to cases with the same equivalence ratio also without water addition but without the

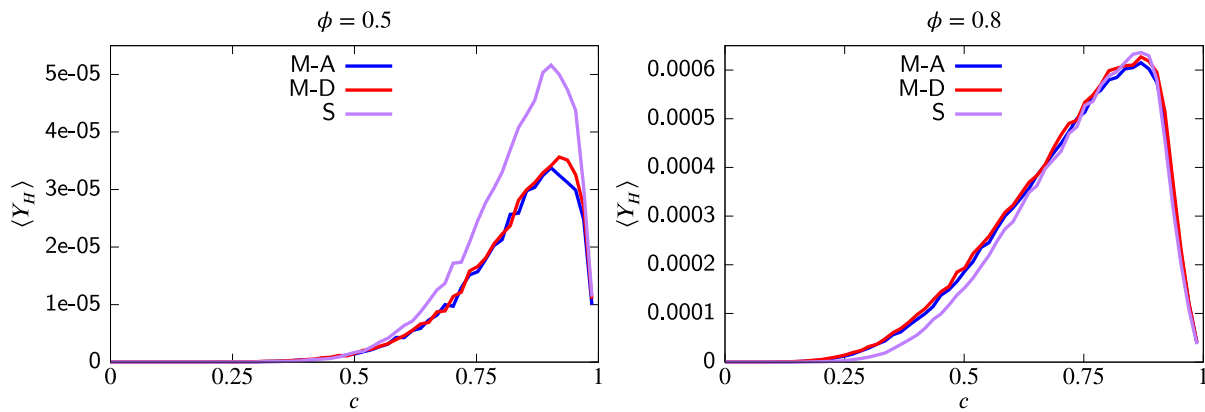


Fig. 6. Average of atomic hydrogen mass fraction $\langle Y_H \rangle$ conditional on the progress variable c for cases with equivalence ratios $\phi = 0.5$ (left) and $\phi = 0.8$ (right) with small water droplets addition $a_d = 7 \mu\text{m}$. The statistics are taken at $t = 0.02 \text{ s}$ for $\phi = 0.5$ and at $t = 0.006 \text{ s}$ for $\phi = 0.8$. The blue curves represent the cases with mixture-averaged diffusion (M-A), the red curves represent the cases with multi-component diffusion (M-D), and the purple curves represent the cases with the inclusion of Soret effect (S). (For interpretation of the references to color in this figure legend, the reader is referred to the web version of this article.)

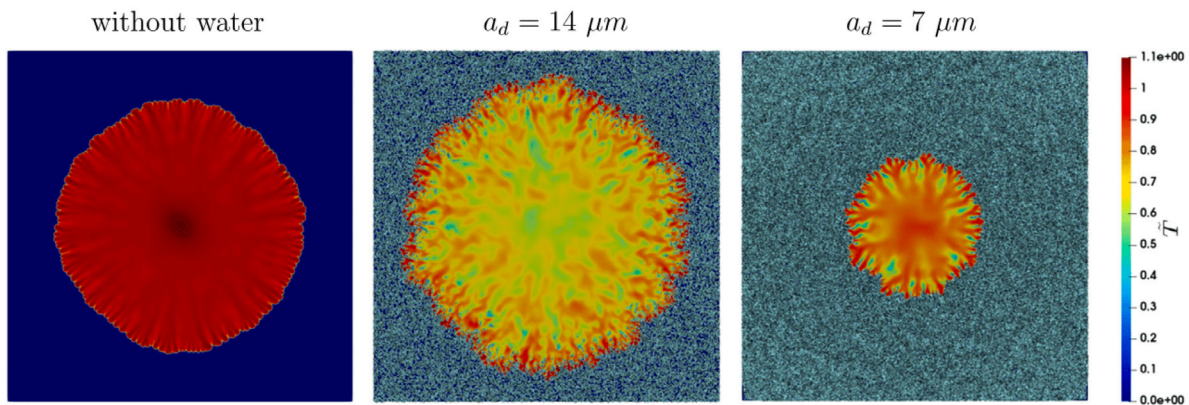


Fig. 7. Normalized temperature field \tilde{T} at $t = 0.02 \text{ s}$ for the cases with equivalence ratio $\phi = 0.5$ including the Soret effect. From left to right, the cases correspond to absent water addition, large water droplets, and small water droplets. The light blue dots indicate the water droplets (not to scale). (For interpretation of the references to color in this figure legend, the reader is referred to the web version of this article.)

Soret effect. The lower H radical concentration characterizes a flame that is locally leaner and propagates at a slower velocity than one with a higher local radical concentration. Conversely, when water droplets are introduced, the radical distribution is significantly altered. Fig. 6 presents the conditional average mass fraction of atomic hydrogen (H) for cases with small water droplets under all diffusion models, for $\phi = 0.5$ (left) and $\phi = 0.8$ (right). It is evident from Fig. 6 that, for $\phi = 0.5$, the Soret effect significantly enhances the mass fraction of H, which becomes substantially higher compared to cases without the Soret effect. In contrast, for $\phi = 0.8$, this effect is much less pronounced, though a slight increase in the peak mass fraction is still observable. However, these results do not fully explain why the leaner case propagates much more slowly with small droplets than without droplets, whereas this behavior is not observed in the $\phi = 0.8$ case, where the two propagation speeds are comparable. The primary reason for this discrepancy lies in the evaporation dynamics. The flame in the $\phi = 0.5$ cases propagates approximately three times slower than in the $\phi = 0.8$ cases, resulting in a prolonged flame-water interaction time, thereby amplifying the cooling effect in the leaner scenario [71].

The differences between the three diffusion models are marginal, particularly between the mixture-averaged and multi-component diffusion models. The latter is the slightly more accurate of the two, especially in terms of describing local flame behavior, but it is also more computationally expensive. Therefore, the choice of model depends on the desired accuracy and the size of the chemical mechanism being used. However, when considering the multi-component diffusion model with the Soret effect, it provides the most complete description of the

flame structure evolution, especially in the context of lean hydrogen/air combustion. For this reason, it will be the only transport model used for the remainder of this work.

4.2. Effects of droplets on propagation characteristics

In this subsection, we focus on comparing the differences in propagation characteristics when initially mono-dispersed droplets with two different droplet sizes are introduced into the domain. As previously observed in Figs. 1, 2, and 3, the initial droplet diameter induces significant differences under the leanest conditions considered (i.e., $\phi = 0.5$). Fig. 2 illustrates a substantial decrease in normalized burning rate per unit area, $\tilde{\Omega}$, when water is added, particularly with smaller droplets. This reduction is primarily attributed to the cooling effect caused by evaporation. Fig. 7 presents the normalized temperature field for the cases with $\phi = 0.5$ for scenarios without water droplets, and with both large and small water droplets. The normalized temperature is defined as:

$$\tilde{T} = \frac{T - T^u}{T_{ad,(\phi)} - T^u} \quad (16)$$

The figure clearly shows the pronounced cooling effect caused by the droplets. In the scenario with large droplets (central panel), the cooling effect is particularly strong in the central part of the flame kernel, yet a spherically expanding flame structure is still evident. Conversely, in the case of small droplets, the cooling effect is prominent at the flame surface, resulting in a more uniform temperature

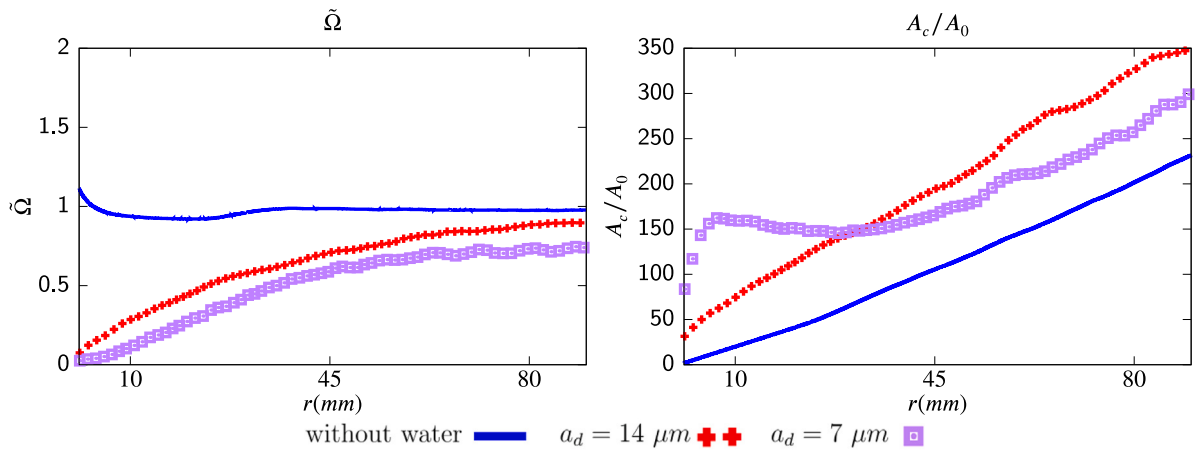


Fig. 8. Evolution of the normalized burning rate per unit area $\tilde{\Omega}$ (left) and non-dimensionalized flame area A_c/A_0 (right) versus flame radius r for cases with equivalence ratio $\phi = 0.8$ and Soret effect inclusion.

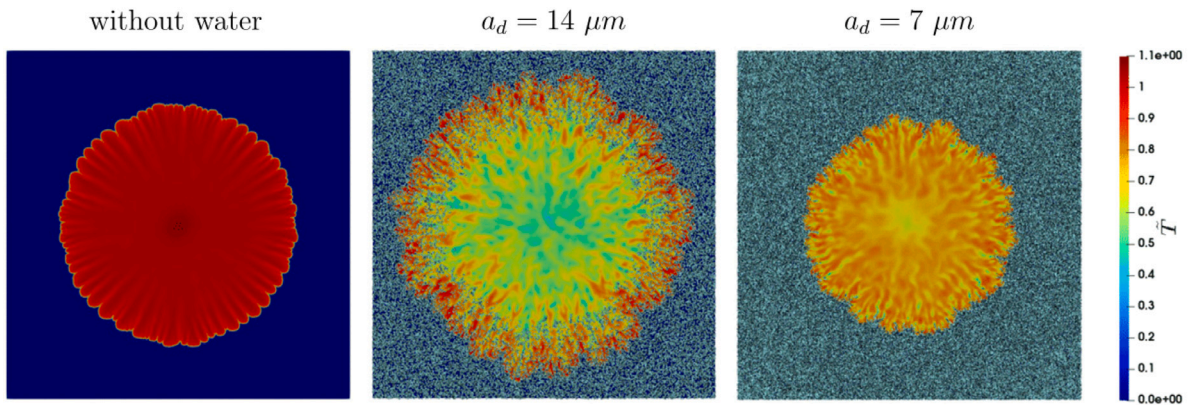


Fig. 9. Normalized temperature field \tilde{T} at $t = 0.006$ s for the cases with equivalence ratio $\phi = 0.8$ including the Soret effect. From left to right, the cases correspond to absent water addition, large water droplets, and small water droplets. The light blue dots indicate the water droplets (not to scale). (For interpretation of the references to color in this figure legend, the reader is referred to the web version of this article.)

distribution in the central burned gas region. However, at the flame surface, distinct regions of cooled gas appear, which correspond to quenched pockets resulting in locally slow flame propagation. Fig. 7 further indicates that the presence of droplets enhances the formation of cellular structures, especially in cases with large water droplets. Similarly, Fig. 4 demonstrates that water addition influences the flame propagation speed in a comparable manner for cases with $\phi = 0.8$ and cases with $\phi = 0.5$. A similar analysis is conducted to assess how the burning rate per unit area and the flame surface area are affected by the interaction with liquid water for the $\phi = 0.8$ case. Fig. 8 depicts the evolution of the normalized burning rate per unit area and the flame area non-dimensionalized with the flame area of the initial kernel at equilibrium conditions, shown on the left and right panels, respectively. Initially, the burning rate per unit area for cases without water addition is close to unity, indicating that preferential diffusion effects are less significant than for $\phi = 0.5$. Furthermore, the impact of water droplets is less pronounced in these cases for both droplet sizes. This reduced impact can be attributed to a shorter interaction time between the flame and the droplets, and the fact that, at $\phi = 0.8$, the flame is more robust and less sensitive to cooling from the liquid phase. Simultaneously, the flame area exhibits a different response to the initial droplet size. During the initial flame development, small droplets generate a larger flame area compared to large droplets. However, as the flame expands, the cooling effect becomes dominant, causing the flame with large droplets to expand faster, resulting in a larger flame area overall. The cooling effect of the droplets in cases with $\phi = 0.8$ is qualitatively visualized in Fig. 9.

As with $\phi = 0.5$, for the case with $\phi = 0.8$ and the addition of small water droplets, the temperature in the central region of the kernel is higher and more uniform than for the case with the addition of large water droplets. On the other side, the flame temperature at the flame front is higher with large droplets, and the temperature in the burned gas region is less uniform and colder than in the other cases with the same equivalence ratio. This different behavior is due to the fact that large droplets are able to penetrate the flame for both equivalence ratios, but more prominently for the $\phi = 0.8$ cases which is characterized by faster flame expansion. At the same time, small droplets are pushed away more easily from the initial position by the flame-induced flow field and evaporate faster than the large droplets. The mass fraction of gaseous water is shown in the appendix, to demonstrate the different droplets' behavior and the dilution effect caused by their evaporation. This behavior can be qualitatively predicted by estimating the ratio between the evaporation time (t_{evap}) and interaction time (t_{int}) for the two different types of droplets. This ratio can be quantified by the expression $t_{evap}/t_{int} = (a_d^2 \rho_d / (8 \rho_b D_{H_2O})) \rho_b \dot{r} / (\rho_u \delta_{th})$, where δ_{th} is the thermal flame thickness, computed as $(T_{ad,\phi} - T_0) / \max(|\nabla T|)$, and D_{H_2O} is the mass diffusivity of water. This ratio is approximately four times higher for large droplets than for small droplets, and it is also influenced by the equivalence ratio, which affects both the thermal flame thickness and the flame radius growth rate \dot{r} . The qualitative observations from Figs. 7 and 9 are quantitatively confirmed by Fig. 10, which represents the probability density function of the normalized temperature \tilde{T} , where the normalization of the temperature is defined

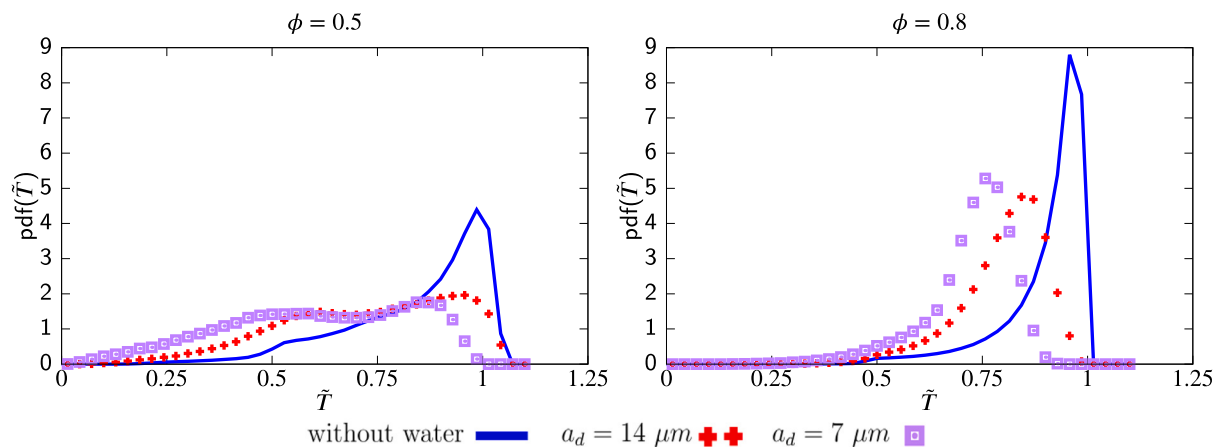


Fig. 10. Probability density function of normalized temperature \tilde{T} for cases with equivalence ratios $\phi = 0.5$ (left) and $\phi = 0.8$ (right), including the Soret effect. The statistics are taken at $t = 0.02$ s for $\phi = 0.5$ and at $t = 0.006$ s for $\phi = 0.8$.

such that the adiabatic flame temperature at the prescribed equivalence ratio gives 1, while the super-adiabatic spots are characterized by $\tilde{T} > 1$.

The thermal stratification is more pronounced at lower equivalence ratios due to preferential diffusion effects, as also investigated in detail in literature [42,72,73]. Consequently, even without droplets, the probability density function (pdf) consistently exhibits a wider distribution, observable through a smaller peak value for the case with $\phi = 0.5$ compared to $\phi = 0.8$. Moreover, it is noteworthy that for $\phi = 0.5$, super-adiabatic spots, which are formed in the location of strongly convex flame surface, (i.e., $\tilde{T} > 1$) are present, whereas for $\phi = 0.8$, there is almost no occurrence of $\tilde{T} > 1$. For both equivalence ratios, the cooling effect behaves similarly with respect to the initial droplet diameter, and in both cases, a shift in the pdf toward lower values of \tilde{T} is observed. However, for $\phi = 0.5$, the distribution becomes slightly wider with the addition of small water droplets compared to large droplets, attributed to the presence of cold, quenching regions along the flame surface. In contrast, for $\phi = 0.8$, the case with small water droplets exhibits reduced thermal stratification, as reflected in the pdf, and achieves a higher peak value than the case with large water droplets.

The addition of water droplets consistently increases the flame area compared to cases without droplets. Among these, the cases with large droplets achieve the highest flame area, surpassing the cases with small droplets after the initial relaxation period. In the $\phi = 0.5$ scenario, the initial period during which the flame area with small droplets is comparable to that of larger droplets lasts until the flame radius reaches approximately 10 mm. For $\phi = 0.8$, this change in behavior occurs at a larger radius, around $r \approx 30$ mm, indicating that the transient duration time is comparable between the two equivalence ratios when considering their respective propagation velocities. The evolution of the flame area in a spherically expanding flame is influenced by two factors: the increase in radius due to the flame kernel expansion and the wrinkling of the flame surface. In the study by Concetti et al. [74], the factor r_A/r was employed to account for the evolution of the wrinkling in a turbulent hydrogen/air spherically expanding flame. In this context, r_A is the radius computed from the flame area ($r_A = A_c/(2\pi)$ note the consistent usage of 3D terminology despite the 2D calculation in this work) using the surface density function. Fig. 11 illustrates the ratio between the radius computed from the flame area r_A and the flame radius r , for cases with different equivalence ratios and its evolution during the flame kernel development. The ratio r_A/r remains above unity for all cases, but in scenarios with droplets addition, the initial values significantly exceed unity due to the initial relaxation of the flame kernel. Notably, r_A/r is slightly higher for $\phi = 0.8$ without water addition and with large droplets compared to the analogous cases at $\phi = 0.5$. This suggests that area generation is higher under conditions that favor hydrodynamic instability than under conditions

dominated by thermodiffusive instability, as confirmed by Berger et al. [65] for planar flames. Moreover, Fig. 11 indicates that the wrinkling is nearly twice as high in the presence of large droplets compared to absence of droplets, while the addition of small droplets results in intermediate wrinkling levels. This outcome is due to the cooling effect, which thickens the flame and makes it less prone to wrinkling, coupled with the lower disturbance intensity compared to the large droplet cases, as observed in literature [42,74]. Fig. 11 also reveals that, in the absence of droplets, the onset of instabilities leads to a wrinkling increase, which occurs at a smaller radius for $\phi = 0.5$ than for $\phi = 0.8$. For cases with droplet addition, a more appropriate metric for observing such trends is the flame area derived from the length of the isocontour of the progress variable, with progress variable value $c = 0.5$. This approach avoids the difficulties of gradients evaluation at the flame kernel's initiation phase for the flame surface density method, which has been used until now because it is more robust and less dependent on the choice of the reaction progress variable [66]. Since the onset of instabilities occurs in the early stages of flame evolution, a closer examination of the initial flame development is necessary. Fig. 12 depicts the ratio between the radius computed from the isocontour length r_A^{iso} and the flame radius r at the initial stage of the flame. The results show that, without droplets, instabilities emerge just before $r = 20$ mm for $\phi = 0.5$ and slightly before $r = 25$ mm for $\phi = 0.8$. In contrast, for large droplet addition, instabilities manifest at approximately $r = 5$ mm for both equivalence ratios. Cases with small droplets are more complex to interpret, but instabilities set in around $r = 1$ mm for $\phi = 0.5$ and around $r = 5$ mm for $\phi = 0.8$. These observations align with the theoretical understanding that hydrogen flames with lower equivalence ratios are more prone to forming cellular structures on the flame surface. Additionally, the presence of droplets acts as a perturbation that leads to formation of wrinkling, as shown by Hasslberger et al. [75] when the evaporation time is small and the average droplet spacing is relatively high compared to the flame characteristics scales. However, the interaction time required for the flame and the penetrating droplets may lead to a larger radius at which instabilities set in, for the cases with $\phi = 0.8$ than for the cases with $\phi = 0.5$, further explaining the observed differences in the onset radius for small droplet cases at different equivalence ratio. The results shown in this section, suggest that under quasi-laminar conditions the droplets favor the initiation of flame instabilities. However, the cooling due to evaporation dampens the symptoms to some extent because of the flame thickening and the decrease of the density jump through the flame which lead to an inhibition of the area generation. These observations are in agreement with the results obtained via simple-chemistry description of similar scenarios under turbulent conditions by Concetti et al. [42,74].

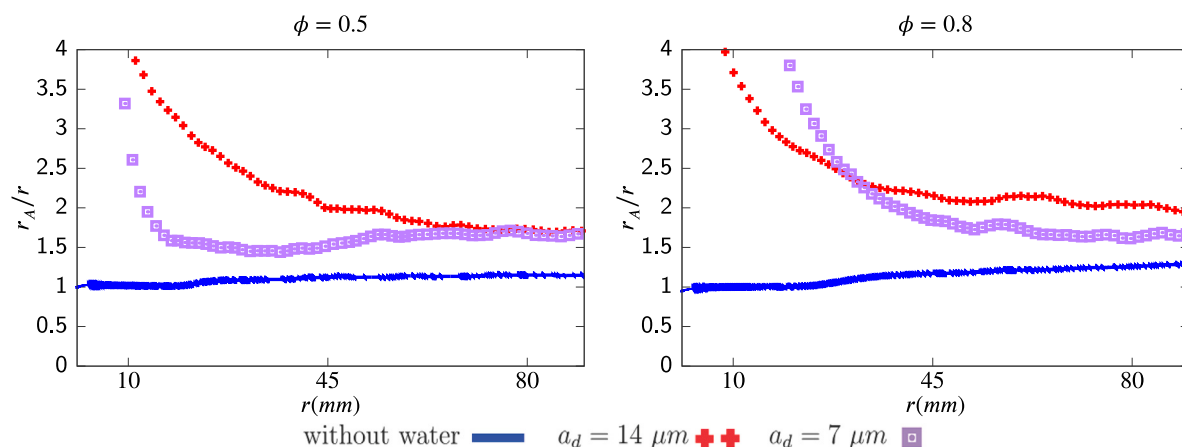


Fig. 11. Evolution of the ratio between the radius based on the area and the flame radius r_A/r versus the flame radius r for the cases with equivalence ratios $\phi = 0.5$ (left) and $\phi = 0.8$ (right), including the Soret effect.

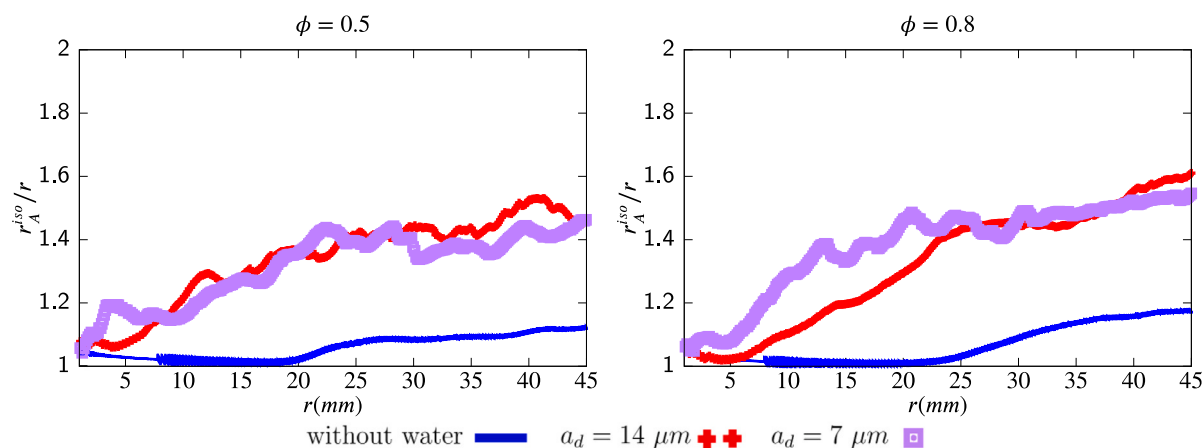


Fig. 12. Evolution of the ratio between the radius computed from the isocontour length and the flame radius r_A^{iso}/r versus the flame radius r for the cases with equivalence ratios $\phi = 0.5$ (left) and $\phi = 0.8$ (right), including the Soret effect.

4.3. Effects of liquid water addition on NO_x emissions

In this section, we present the results of a series of simulations using a chemical mechanism that incorporates nitrogen chemistry [60–62]. The mechanism employed includes 31 species and 203 elementary reactions, significantly increasing computational cost relative to simulations conducted with the previous mechanism [59]. Consequently, only a quarter of the domain has been simulated, due to the problem's symmetry. The objective here is to analyze the effects of liquid water injection on NO_x production, with particular attention to NO formation, being the most relevant one among the NO_x species. As previously mentioned, nitrogen oxides in hydrogen/air combustion are primarily formed through three pathways: the thermal, N_2O , and NNH pathways. The thermal pathway, as suggested by its name, is highly temperature-dependent and is the dominant formation route when the temperature exceeds 1800 K [37,76–78]. The N_2O pathway is associated with high concentrations of atomic oxygen and is initiated through third-body reactions, making it particularly active under high pressure or in the presence of strong colliders (e.g., water vapor). Moreover, the low activation energy of the initial reaction renders the N_2O pathway relatively insensitive to temperature, allowing NO production even at low combustion temperatures (e.g., extremely lean conditions) [78,79]. Finally, the NNH pathway is also related to high concentrations of O and H radicals, as the N_2O pathway, but is more prominent under rich conditions. In lean scenarios, pathway conversion tends to occur, with NNH reacting with O to produce N_2O [79].

The flame with $\phi = 0.5$ is characterized by a maximum temperature below 1800 K. Under these conditions, thermal NO_x production is inhibited. Fig. 13 illustrates the Y_{NO} fields for cases with $\phi = 0.5$ without droplets and with the addition of large and small water droplets, at a flame radius of $r \approx 0.065$ m. It is evident that water addition enhances NO production. At this equivalence ratio, the thermal NO_x pathway is weak and incapable of producing substantial NO. Therefore, the cooling effect from water evaporation does not suppress NO production; rather, it appears to increase it. To explore the pathways contributing to NO generation, it is useful to examine fields of other relevant chemical species near the regions with high NO concentrations. Fig. 14 shows the mass fractions of NO, H_2O and N_2O for the case with $\phi = 0.5$ and the addition of large water droplets, providing qualitative insights into the mechanisms driving NO formation and confirming the significant effect of water.

Comparing these fields reveals that regions of high NO concentration coincide precisely with the evaporation sites of the droplets, these “cold spots” are characterized by locally higher H_2O concentrations and low temperatures. Additionally, these high NO concentration regions are located in areas with elevated N_2O concentrations. This observation suggests that, at low equivalence ratios, the addition of liquid water activates the N_2O pathway due to water's high collision efficiency and the temperature insensitivity of this reaction pathway. The reduced intensity of NO production observed with smaller water droplets in Fig. 13 is due to less stratification of temperature and water vapor, resulting from the shorter evaporation time associated with smaller

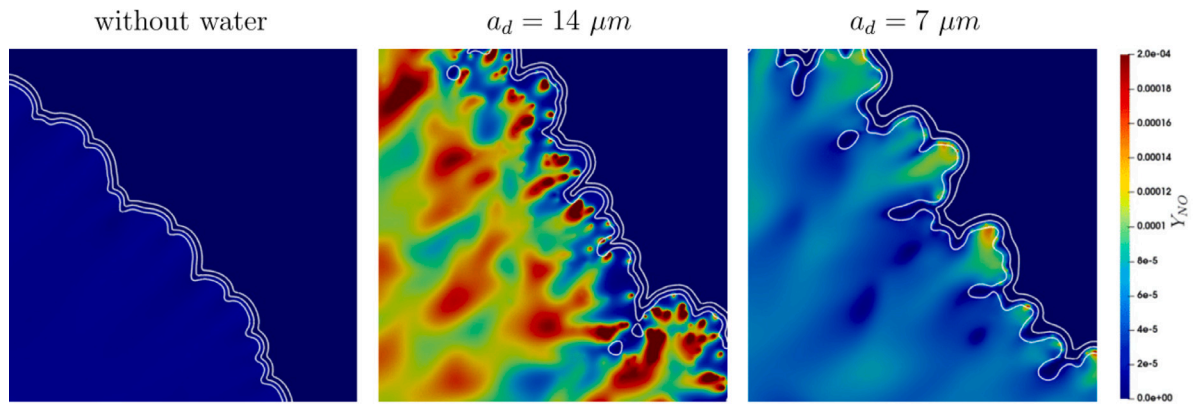


Fig. 13. Magnified view close to the flame front of nitrogen monoxide mass fraction Y_{NO} for the cases with equivalence ratio $\phi = 0.5$, including the Soret effect, with equal flame radius $r \approx 0.065$ m. From left to right, the cases correspond to absent water addition, large water droplets, and small water droplets. The white lines represent the iso-contour with $c = 0.05, 0.5$ and 0.95 . (For interpretation of the references to color in this figure legend, the reader is referred to the web version of this article.)

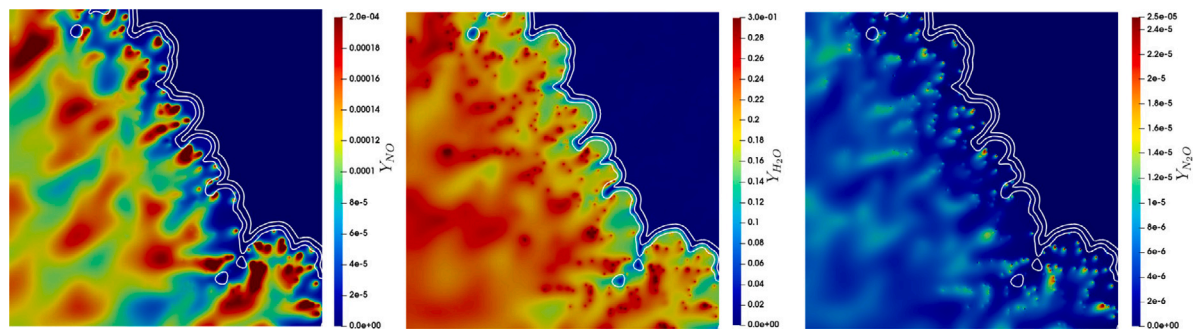


Fig. 14. Magnified view close to the flame front of nitrogen monoxide mass fraction Y_{NO} (left), water mass fraction Y_{H_2O} (center) and nitrous oxide mass fraction Y_{N_2O} (right) fields for the case with equivalence ratio $\phi = 0.5$, including the Soret effect and large water droplets addition, with flame radius $r \approx 0.065$ m. The white lines represent the iso-contour with $c = 0.05, 0.5$ and 0.95 . (For interpretation of the references to color in this figure legend, the reader is referred to the web version of this article.)

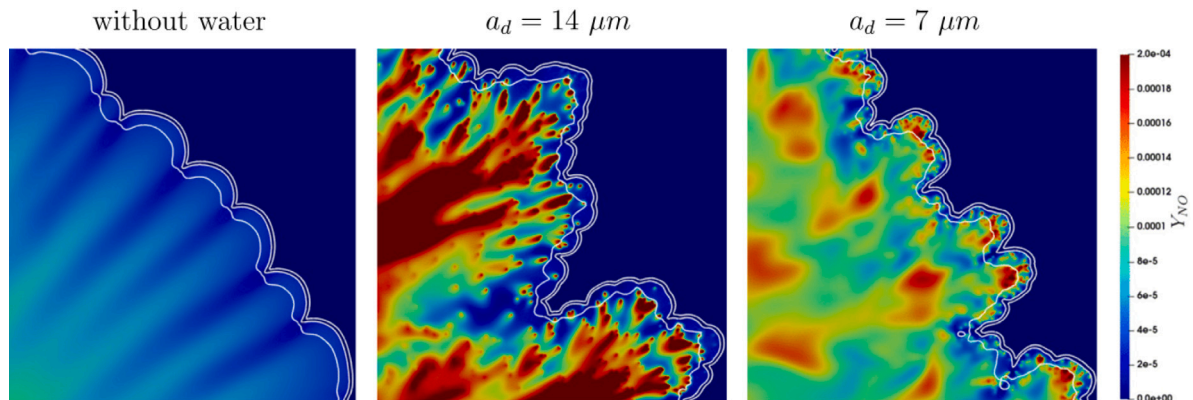


Fig. 15. Magnified view close to the flame front of nitrogen monoxide mass fraction Y_{NO} for the cases with equivalence ratio $\phi = 0.8$, including the Soret effect, with equal flame radius $r \approx 0.065$ m. From left to right, the cases correspond to absent water addition, large water droplets, and small water droplets. The white lines represent the iso-contour with $c = 0.05, 0.5$ and 0.95 . (For interpretation of the references to color in this figure legend, the reader is referred to the web version of this article.)

initial diameters. This leads to greater overall evaporation but lower local concentrations, thereby diminishing the enhancement of the N_2O pathway. The NNH pathway is omitted from this discussion, as local peaks of mass fraction are several orders of magnitude lower than those of N_2O .

As the equivalence ratio increases, the system's maximum temperature also rises. At the same time, radical concentrations and overall flame structure are impacted, as previously discussed in this work. These changes are expected to influence NO formation processes and, consequently, the effects of water addition on emissions. Fig. 15 presents the NO fields for cases with $\phi = 0.8$, showing configurations without

water addition, large water droplets, and small water droplets. At this equivalence ratio, the case with large water droplets produces the highest NO levels. Meanwhile, the case with small water droplets produces slightly more nitrogen monoxide than the case without water addition, though the increase is less pronounced than at lower equivalence ratios. At $\phi = 0.8$, the maximum temperature exceeds the threshold of 1800 K, explaining the overall increased NO production compared to $\phi = 0.5$. However, the thermal pathway operates on a longer timescale than other pathways (on the order of hundreds of milliseconds [78]). Consequently, the configuration results in a peak thermal NO concentration at the center of the flame kernel rather than the flame front. The high

NO concentration branches (red spots in Figs. 13 and 15) originating from the flame front and extending toward the central region are primarily associated with other formation pathways, especially the N_2O pathway. This observation suggests that, in the absence of droplets, most NO production arises from the thermal route since there are no visible branches that are related to the N_2O pathway. In contrast, for the case with large water droplets, NO formation is dominated by radical-driven pathways, particularly the N_2O pathway, as indicated by the branches beginning near evaporation sites. Finally, in the case with small water droplets, an intermediate situation emerges, with both the N_2O and thermal pathways contributing to NO production. This is due to the more uniform effects of water.

Based on the presented results, it can be concluded that regulating NO_x emissions through water addition requires careful design and is highly dependent on the considered flame configuration. In the case of laminar, spherically expanding flames, NO emissions are slightly increased under the lean combustion conditions investigated in this study. However, in scenarios with a turbulent velocity field and greater droplet mobility, it has been observed that cooling would likely occur in different regions of the flame [42,71,74,75], leading to altered conditions for NO formation. This might explain why, in practical applications such as diesel engines and gas turbine combustors, liquid water injection typically reduces NO_x emissions [7]. Moreover these observations have been made in experimental context, which are characterized by other complexities (e.g., non-uniformity of fuel concentration, polydisperse droplet size distributions) which further affect the NO formation.

5. Conclusions

In this study, the impact of liquid water addition on hydrogen/air laminar premixed flames has been investigated, with a focus on variations in diffusion model, equivalence ratio, and initial water droplet diameter. It has been found that:

- The inclusion of the Soret effect has moderate effects. For $\phi = 0.5$, an enhancement in the formation of cellular structures is observed when the Soret effect is included, leading to a faster radial expansion of the flame kernel.
- For the cases with $\phi = 0.8$, the inclusion of the Soret effect results in a flame that is less prone to instability and exhibits a slower radial expansion compared to cases without the Soret effect.
- With water addition, particularly through small water droplets, the Soret effect increases the flame's susceptibility to instability and cellular structure formation, even for $\phi = 0.8$. Water evaporation affects the radical distribution inside the flame, particularly the light radicals such as H, which in turn influences flame stability and propagation characteristics.

Based on these observations, it is suggested to include the Soret effect in the diffusion model, as it more accurately captures the phenomenology and flame structure evolution, particularly when diffusion plays a significant role in the system's dynamics. Regarding the propagation characteristics, it has been observed that:

- The radial growth of spherically expanding hydrogen/air premixed flames is enhanced by the addition of large water droplets, while the addition of small water droplets attenuates the growth. This observation holds for both equivalence ratios investigated in the present work.
- The droplets act as localized disturbances, triggering the formation of cellular structures and enhancing the growth of the flame area. On the other hand, water evaporation lowers the system's temperature, resulting in a reduction of the burning rate per unit area of the flame. For large water droplets, the enhancement of flame area generation dominates over the cooling effect. Conversely, when small droplets are added, the decrease in the

burning rate per unit area outweighs the flame area enhancement, leading to a reduced flame consumption speed and consequently radial growth compared to the case without water droplets.

- When the equivalence ratio is $\phi = 0.8$, the reduction in flame consumption speed with the addition of small droplets is less significant than for $\phi = 0.5$. This occurs because the droplet-flame interaction time is shorter for $\phi = 0.8$ than for $\phi = 0.5$.

Finally, the analysis of NO_x emissions has shown:

- The formation of NO_x with $\phi = 0.5$ is primarily due to the N_2O pathway, as the maximum temperature reached is below 1800 K, where the thermal pathway is less significant. Therefore, the cooling effect associated with water addition has a limited impact on reducing NO formation. However, it increases the local concentration of H and O radicals, which enhances the intensity of the N_2O pathway. Furthermore, this pathway begins with a third-body reaction that has a low activation energy, making it largely temperature-independent and driven by the high collision efficiency of water molecules. As a result, NO formation is localized around the “cold spots” generated by droplet evaporation.
- For the cases with $\phi = 0.8$, the thermal pathway becomes more relevant. However, water droplet evaporation increases radical concentrations, which strengthens the N_2O pathway. Thus, for this equivalence ratio, the addition of large water droplets also leads to an increase in NO formation around the “cold spots”.
- In the case with small droplet addition and $\phi = 0.8$, there is a slight increase in NO concentration compared to the case without water addition at the same equivalence ratio. However, this increase is marginal when compared to the higher NO concentrations observed with large water droplets. This occurs because evaporation of small droplets is rapid and almost complete ahead of the flame, where there is a lower concentration of radicals. These conditions do not provide sufficient amplification of the N_2O pathway strength.

In the configurations examined in this study, the addition of liquid water has been shown to increase NO_x emissions, contrasting with findings from studies in the literature that examine scenarios with different flame configurations. This discrepancy might arise because, in those scenarios where turbulence or droplet mobility is higher than in the cases considered in the present work, the effects of the droplets affect the flame in different regions, which in turn influences NO production in a different manner. Therefore, if this technique has to be considered as a potential method for emission reduction, careful system design must account for all effects arising from droplet-flame interactions besides effects related to wall confinement, mixture non-uniformity and polydisperse droplet size distributions. Since this work aimed to investigate different aspects of quasi-laminar flames interacting with droplets, turbulent flow conditions have not been considered to avoid masking effects. However, it is worthwhile to investigate the effects of liquid water addition on emissions in turbulent premixed flames in the future.

CRediT authorship contribution statement

Riccardo Concetti: Writing – original draft, Visualization, Software, Methodology, Investigation, Formal analysis, Data curation, Conceptualization. **Josef Hasslberger:** Writing – review & editing, Supervision, Software, Methodology. **Markus Klein:** Writing – review & editing, Supervision, Resources, Project administration, Methodology, Funding acquisition.

Declaration of competing interest

The authors declare that they have no known competing financial interests or personal relationships that could have appeared to influence the work reported in this paper.

Acknowledgments

This research, in the frame of project MORE, is funded by dtec.bw – Digitalization and Technology Research Center of the Bundeswehr, Germany which we gratefully acknowledge. dtec.bw is funded by the European Union – NextGenerationEU.

Appendix A. Supplementary data

Supplementary material related to this article can be found online at <https://doi.org/10.1016/j.ijhydene.2025.02.286>.

References

- Li A, Zheng Z, Peng T. Effect of water injection on the knock, combustion, and emissions of a direct injection gasoline engine. *Fuel* 2020;268:117376.
- Görgülü A, Yağlı H, Koç Y, Koç A. Comprehensive analysis of the effect of water injection on performance and emission parameters of the hydrogen fuelled recuperative and non-recuperative gas turbine system. *Int J Hydrog Energy* 2020;45:34254–67.
- Ni P, Wang X, Li H. A review on regulations, current status, effects and reduction strategies of emissions for marine diesel engines. *Fuel* 2020;279:118477.
- Concetti R, Hasslberger J, Sattelmayer T, Klein M. On the chemical effect of steam addition to premixed hydrogen flames with respect to NO_x emissions and flame speed. *Flow, Turbul Combust* 2024;1–16.
- Lellek S. Pollutant formation in premixed natural gas swirl flames with water injection [Ph.D. thesis], Technische Universität München; 2017.
- Reale F, Sannino R. Water and steam injection in micro gas turbine supplied by hydrogen enriched fuels: Numerical investigation and performance analysis. *Int J Hydrog Energy* 2021;46:24366–81.
- Lellek S, Sattelmayer T. NO_x-formation and CO-burnout in water-injected, premixed natural gas flames at typical gas turbine combustor residence times. *J Eng Gas Turbines Power* 2018;140:051504.
- Shibue K, Sugiyama Y, Matsuo A. Numerical study of the effect on blast-wave mitigation of the quasi-steady drag force from a layer of water droplets sprayed into a confined geometry. *Process Saf Environ Prot* 2022;160:491–501.
- Liu Z, Zhong X, Zhang Q, Lu C. Experimental study on using water mist containing potassium compounds to suppress methane/air explosions. *J Hazard Mater* 2020;394:122561.
- Aniello A, Poinso T, Selle L, Schuller T. Hydrogen substitution of natural-gas in premixed burners and implications for blow-off and flashback limits. *Int J Hydrog Energy* 2022;47:33067–81.
- Mira D, Lehmkuhl O, Both A, Stathopoulos P, Tanneberger T, Reichel TG, Paschereit CO, Vázquez M, Houzeaux G. Numerical characterization of a premixed hydrogen flame under conditions close to flashback. *Flow, Turbul Combust* 2020;104:479–507.
- Pappa A, Bricteux L, Bénard P, De Paepe W. Can water dilution avoid flashback on a hydrogen-enriched micro-gas turbine combustion?—a large eddy simulations study. *J Eng Gas Turbines Power* 2021;143:041008.
- Matalon M. Intrinsic flame instabilities in premixed and nonpremixed combustion. *Annu Rev Fluid Mech* 2007;39:163–91.
- Darrieus G. Propagation d'un front de flamme la technique moderne (Paris) and in 1945 at congrès de mécanique appliquée. Unpubl Work 1938.
- Landau L. On the theory of slow combustion. In: *Dynamics of curved fronts*. Elsevier; 1988, p. 403–11.
- Markstein GH. Experimental and theoretical studies of flame-front stability. In: *Dynamics of curved fronts*. Elsevier; 1988, p. 413–23.
- Clavin P, Williams F. Effects of molecular diffusion and of thermal expansion on the structure and dynamics of premixed flames in turbulent flows of large scale and low intensity. *J Fluid Mech* 1982;116:251–82.
- Pelce P, Clavin P. Influence of hydrodynamics and diffusion upon the stability limits of laminar premixed flames. In: *Dynamics of curved fronts*. Elsevier; 1988, p. 425–43.
- Matalon M, Matkowsky B. Flames as gasdynamic discontinuities. *J Fluid Mech* 1982;124:239–59.
- Matalon M, Matkowsky B. On the stability of plane and curved flames. *SIAM J Appl Math* 1984;44:327–43.
- Michelson DM, Sivashinsky GI. Nonlinear analysis of hydrodynamic instability in laminar flames—II. Numerical experiments. *Acta Astronaut* 1977;4:1207–21.
- Sivashinsky G. Nonlinear analysis of hydrodynamic instability in laminar flames—I. Derivation of basic equations. In: *Dynamics of curved fronts*. Elsevier; 1988, p. 459–88.
- Sivashinsky GI. Instabilities, pattern formation, and turbulence in flames. *Ann Rev Fluid Mech* 1983;15:179–99.
- Berger L, Attili A, Pitsch H. Intrinsic instabilities in premixed hydrogen flames: Parametric variation of pressure, equivalence ratio, and temperature. part 1—dispersion relations in the linear regime. *Combust Flame* 2022;240:111935.
- Li T, Wang X, Ma Y, Wang L, Oppong F, Xu C, Jiang G. Investigation on hydrogen/ethanol intrinsic flame instability. *Combust Flame* 2022;241:112064.
- D'Alessio F, Matteucci C, Lapenna P, Creta F. Intrinsic instability of lean hydrogen/ammonia premixed flames: Influence of Soret effect and pressure. *Fuel Commun* 2024;19:100110.
- Law CK, Jomaas G, Bechtold JK. Cellular instabilities of expanding hydrogen/propane spherical flames at elevated pressures: theory and experiment. *Proc Combust Inst* 2005;30:159–67.
- Jomaas G, Law CK, Bechtold J. On transition to cellularity in expanding spherical flames. *J Fluid Mech* 2007;583:1–26.
- Addabbo R, Bechtold J, Matalon M. Wrinkling of spherically expanding flames. *Proc Combust Inst* 2002;29:1527–35.
- Kim W, Sato Y, Johzaki T, Endo T, Shimokuri D, Miyoshi A. Experimental study on self-acceleration in expanding spherical hydrogen-air flames. *Int J Hydrog Energy* 2018;43:12556–64.
- Yang S, Saha A, Wu F, Law CK. Morphology and self-acceleration of expanding laminar flames with flame-front cellular instabilities. *Combust Flame* 2016;171:112–8.
- Nicoli C, Haldenwang P, Denet B. Premixed flame dynamics in presence of mist. *Combust Sci Technol* 2019;191:197–207.
- Grear JF, Bell JB, Day MS. The Soret effect in naturally propagating, premixed, lean, hydrogen-air flames. *Proc Combust Inst* 2009;32:1173–80.
- Korsakova A, Gubernov V, Bykov V, Maas U. The effect of Soret diffusion on stability of rich premixed hydrogen-air flames. *Int J Hydrog Energy* 2016;41:17670–5.
- Schlup J, Blanquart G. Validation of a mixture-averaged thermal diffusion model for premixed lean hydrogen flames. *Combust Theory Model* 2018;22:264–90.
- Zhou Z, Hernández-Pérez FE, Shoshin Y, van Oijen JA, de Goey LP. Effect of Soret diffusion on lean hydrogen/air flames at normal and elevated pressure and temperature. *Combust Theory Model* 2017;21:879–96.
- Wen X, Berger L, Cai L, Parente A, Pitsch H. Thermodynamically unstable laminar hydrogen flame in a sufficiently large 3D computational domain—Part II: NO_x formation mechanism and flamelet modeling. *Combust Flame* 2024;265:113497.
- Göckeler K. Influence of steam dilution and hydrogen enrichment on laminar premixed methane flames. Technische Universität Berlin (Germany); 2015.
- Reveillon J, Vervisch L. Analysis of weakly turbulent dilute-spray flames and spray combustion regimes. *J Fluid Mech* 2005;537:317–47.
- Wacks DH, Chakraborty N. Statistical analysis of the reaction progress variable and mixture fraction gradients in flames propagating into droplet mist: a direct numerical simulation analysis. *Combust Sci Technol* 2016;188:2149–77.
- Angellilli L, Hernández Pérez FE, Im HG, Ciottoli PP, Valorani M. Evaporation and clustering of ammonia droplets in a hot environment. *Phys Rev Fluids* 2022;7:114301.
- Concetti R, Hasslberger J, Chakraborty N, Klein M. Effects of liquid water addition on turbulent premixed hydrogen/air combustion. *Fuel* 2024;373:132314.
- Hirschfelder J, Curtiss C. Theory of propagation of flames. Part I: General equations. In: *Symposium on combustion and flame, and explosion phenomena*, vol. 3. Elsevier; 1948, p. 121–7.
- Bird RB, Klingenberg DJ. Multicomponent diffusion—A brief review. *Adv Water Resour* 2013;62:238–42.
- Ern A, Giovangigli V. Thermal diffusion effects in hydrogen-air and methane-air flames. *Combust Theory Model* 1998;2:349.
- Ern A, Giovangigli V. Impact of detailed multicomponent transport on planar and counterflow hydrogen/air and methane/air flames. *Combust Sci Technol* 1999;149:157–81.
- Yang F, Law CK, Sung C, Zhang H. A mechanistic study of Soret diffusion in hydrogen-air flames. *Combust Flame* 2010;157:192–200.
- Kee RJ, Coltrin ME, Glarborg P. *Chemically reacting flow: theory and practice*. John Wiley & Sons; 2005.
- Crowe CT, Schwarzkopf JD, Sommerfeld M, Tsuji Y. *Multiphase flows with droplets and particles*. CRC Press; 2011.
- Ranz W, Marshall W. Evaporation from droplets. *Chem Eng Prog* 1952;48:141–6.
- Yuen M, W. CL. On drag of evaporating liquid droplets. 1976.
- Abramzon B, Sirignano WA. Droplet vaporization model for spray combustion calculations. *Int J Heat Mass Transfer* 1989;32:1605–18.
- Van Oijen J, Donini A, Bastiaans R, ten Thije Boonkkamp J, De Goey L. State-of-the-art in premixed combustion modeling using flamelet generated manifolds. *Prog Energy Combust Sci* 2016;57:30–74.
- Papapostolou V, Chakraborty N, Klein M, Im HG. Effects of reaction progress variable definition on the flame surface density transport statistics and closure for different combustion regimes. *Combust Sci Technol* 2019.
- Wehrmann VS, Chakraborty N, Klein M, Hasslberger J. Choice of reaction progress variable under preferential diffusion effects in turbulent syngas combustion based on detailed chemistry direct numerical simulations. *Sci Rep* 2024;14:14861.
- Zirwes T, Zhang F, Habisreuther P, Hansinger M, Bockhorn H, Pfitzner M, Trimis D. Quasi-DNS dataset of a piloted flame with inhomogeneous inlet conditions. *Flow, Turbul Combust* 2020;104:997–1027.

- [57] Greenshields C, Weller H. Notes on computational fluid dynamics: General principles. Reading, UK: CFD Direct Ltd; 2022.
- [58] Goodwin DG, Moffat HK, Schoegl I, Speth RL, Weber BW. Cantera: An object-oriented software toolkit for chemical kinetics, thermodynamics, and transport processes. 2023, Version 3.0.0, <https://www.cantera.org>.
- [59] Li J, Zhao Z, Kazakov A, Dryer FL. An updated comprehensive kinetic model of hydrogen combustion. *Int J Chem Kinet* 2004;36:566–75.
- [60] Song Y, Marrodán L, Vin N, Herbinet O, Assaf E, Fittschen C, Stagni A, Faravelli T, Alzueta MU, Battin-Leclerc F. The sensitizing effects of NO₂ and NO on methane low temperature oxidation in a jet stirred reactor. *Proc Combust Inst* 2019;37:667–75.
- [61] Stagni A, Cavallotti C, Arunthanayothin S, Song Y, Herbinet O, Battin-Leclerc F, Faravelli T. An experimental, theoretical and kinetic-modeling study of the gas-phase oxidation of ammonia. *React Chem Eng* 2020;5:696–711.
- [62] Stagni A, Arunthanayothin S, Dehue M, Herbinet O, Battin-Leclerc F, Bréquigny P, Mounaim-Rousselle C, Faravelli T. Low-and intermediate-temperature ammonia/hydrogen oxidation in a flow reactor: Experiments and a wide-range kinetic modeling. *Chem Eng J* 2023;471:144577.
- [63] Gai G, Kudriakov S, Rogg B, Hadjadj A, Studer E, Thomine O. Numerical study on laminar flame velocity of hydrogen-air combustion under water spray effects. *Int J Hydrog Energy* 2019;44:17015–29.
- [64] Poinot T. Theoretical and numerical combustion. RT Edwards 2005.
- [65] Berger L, Grinberg M, Jürgens B, Lapenna PE, Creta F, Attili A, Pitsch H. Flame fingers and interactions of hydrodynamic and thermodynamic instabilities in laminar lean hydrogen flames. *Proc Combust Inst* 2023;39:1525–34.
- [66] Klein M, Herbert A, Kosaka H, Böhm B, Dreizler A, Chakraborty N, Papapostolou V, Im HG, Hasslberger J. Evaluation of flame area based on detailed chemistry DNS of premixed turbulent hydrogen-air flames in different regimes of combustion. *Flow, Turbul Combust* 2020;104:403–19.
- [67] Damköhler G. Der einfluss der turbulenz auf die flammengeschwindigkeit in gasgemischen. *Zeitschrift für Elektrochemie und Angewandte Physikalische Chemie* 1940;46:601–26.
- [68] Chakraborty N, Alwazzan D, Klein M, Cant RS. On the validity of Damköhler's first hypothesis in turbulent Bunsen burner flames: A computational analysis. *Proc Combust Inst* 2019;37:2231–9.
- [69] Mitani T, Williams F. Studies of cellular flames in hydrogen/oxygen/nitrogen mixtures. *Combust Flame* 1980;39:169–90.
- [70] Bell JB, Cheng RK, Day MS, Shepherd IG. Numerical simulation of Lewis number effects on lean premixed turbulent flames. *Proc Combust Inst* 2007;31:1309–17.
- [71] Concetti R, Hasslberger J, Chakraborty N, Klein M. Analysis of water droplet interaction with turbulent premixed and spray flames using carrier phase direct numerical simulations. *Combust Sci Technol* 2023;195:1411–33.
- [72] Varea E, Beekmann J, Pitsch H, Chen Z, Renou B. Determination of burning velocities from spherically expanding H₂/air flames. *Proc Combust Inst* 2015;35:711–9.
- [73] Berger L, Attili A, Pitsch H. Intrinsic instabilities in premixed hydrogen flames: parametric variation of pressure, equivalence ratio, and temperature. Part 2 – Non-linear regime and flame speed enhancement. *Combust Flame* 2022;240:111936.
- [74] Concetti R, Hasslberger J, Chakraborty N, Klein M. Effects of water mist on the initial evolution of turbulent premixed hydrogen/air flame kernels. *Energies* 2024;17:4632.
- [75] Hasslberger J, Ozel-Erol G, Chakraborty N, Klein M, Cant S. Physical effects of water droplets interacting with turbulent premixed flames: a direct numerical simulation analysis. *Combust Flame* 2021;229:111404.
- [76] Correa SM. A review of NO_x formation under gas-turbine combustion conditions. *Combust Sci Technol* 1993;87:329–62.
- [77] Day MS, Bell JB, Gao X, Glarborg P. Numerical simulation of nitrogen oxide formation in lean premixed turbulent H₂/O₂/N₂ flames. *Proc Combust Inst* 2011;33:1591–9.
- [78] Joos F. Technische Verbrennung, vol. 76. Springer; 2006.
- [79] Capurso T, Laera D, Riber E, Cuenot B. NO_x pathways in lean partially premixed swirling H₂-air turbulent flame. *Combust Flame* 2023;248:112581.